A numerical study on frictional shakedown in large-scale three-dimensional conforming elastic contacts

A numerical study on frictional shakedown in large-scale three-dimensional conforming elastic contacts

A. Spagnoli[a,*], G. Beccarelli[a], M. Terzano[a,b], J. R. Barber[a]

[a] *Department of Engineering and Architecture, University of Parma, Parco Area delle Scienze 181/A, 43124 Parma, Italy*
[b] *Department of Mechanical Engineering, Imperial College London, Exhibition Road, London SW7 2AZ, UK*
[c] *Department of Mechanical Engineering, University of Michigan, Ann Arbor, USA*

Abstract

When subjected to cyclic loading, complete contacts with *à la* Coulomb friction may sometimes develop a favourable situation where slips cease after a few cycles, an occurrence commonly known as frictional shakedown. However, if the amplitude of the cyclic load is greater than a so-called shakedown limit, the system is unable to adapt and indefinitely persists in a dissipative state. In this paper, we present a comprehensive theoretical and numerical analysis of the shakedown in three-dimensional elastic systems with conforming frictional interfaces. In a discrete framework, the limit states of the frictional system are investigated through two distinct approaches: incremental analysis based on a novel Gauss-Seidel algorithm, which allowed us to explore the whole transient response under a given cyclic loading scenario, and a linear optimisation algorithm to directly determine the stick and shakedown limits. Illustrative examples, ranging from a single-node model to multi-node systems with both coupled and uncoupled contacts, are discussed.

*Corresponding author. Tel.: +39-0521-905927; fax: +39-0521-905924;
e-mail: spagnoli@unipr.it.

Keywords: Shakedown; Friction; Contact; Limit analysis; Linear programming

1. Introduction

Engineering systems often comprise several parts interacting through frictional contact, some of which are subjected to a combination of a static load and time varying cyclic actions, e.g due to vibrations or temperature fluctuations (Andresen et al., 2019). As a consequence of these actions, contacts experience frictional slip in terms of small relative tangential displacements along the contact interface, whose effect on the performance of the engineering part is usually detrimental. Fretting fatigue, for instance, is the well-known damage process resulting from zones of micro-slip between contacting interfaces, which leads to the initiation of cracks, thereby significantly reducing the service life of components (Nowell et al., 2006; Majzoobi and Abbasi, 2017). A particularly amenable condition is known from the theory of plasticity: it may happen that, after a certain number of cycles in which the system shows an inelastic response, the behaviour in the subsequent loading cycles becomes purely elastic (König and Maier, 1981). This condition of adaptation goes under the name of shakedown. A similar phenomenon has been observed in assemblies comprising elastic components in mutual contact, following the analogy between slips and plastic strains (Churchman et al., 2006; Antoni, 2017): after a transient response where slip may develop along limited portions of the contact interface, a state of permanent stick with non-dissipative behaviour is eventually attained. It is therefore of great importance to investigate such a safe condition, commonly known as frictional shakedown (Carpinteri and Scavia, 1993; Churchman and Hills, 2006).

Conforming or complete contacts, i.e. those in which the contact area does not change in the presence of applied loads or becomes smaller in case of receding contacts (Ahn and Barber, 2008), are preferably avoided in engineering practice. Indeed, differently from incomplete contacts that have non-conforming interfaces and smooth edges (Fleury et al., 2017), the presence of sharp features results in large stress concentration. Due to the lack of closed-form solutions, complete contacts are typically studied through a combination of numerical analyses and asymptotic methods (Flicek et al., 2015b). The response of conforming contacts subjected to constant normal load and variable tangential forces has been analysed in several geometries, including the notable cases of a rigid or elastic punch pressed onto an elastic half-plane (Mugadu and Hills, 2003; Churchman and Hills, 2006) and the contact between circular interfaces in pin-loaded lugs (Antoni, 2014). Evidences have been found showing that, under a combination of constant and cyclic quasi-static loads, frictional shakedown might develop, an occurrence which is prevented in incomplete contacts where micro-slips at the edges are almost always present. Known exceptions are cases where an inclined oscillating force forms an angle with respect to the normal to the contact plane smaller than the angle of friction, while the normal load is constant (Barber et al., 2008). Following the traditional framework of limit analysis applied to elastic-plastic systems, shakedown theorems for frictional contacts have been formulated in discrete and continuum problems (Klarbring et al., 2007; Barber et al., 2008; Klarbring et al., 2017). In particular, the analogous of Melan's static theorem establishes a sufficient condition for shakedown based on the existence of a safe residual slip distribution that prevents dissipation at all times during the steady state (Klarbring et al.,

2007). Regretfully, Coulomb's law, and more generally any pressure-dependent frictional formulation with non-associated flow, limits the existence of such a theorem to cases in which the normality rule is retained (Drucker, 1954). In complete contacts, this occurs when there is no coupling between normal and tangential directions on the slip surface (Klarbring et al., 2007), so that the normal components can be regarded as determined from equilibrium alone while the normality rule is respected on the tangential plane (Michalowski and Mroz, 1978). In all other cases, the steady-state response depends on the initial residual slip distribution (Ahn et al., 2008; Ahn, 2015). Melan's theorem does not provide a sufficient condition for shakedown in coupled systems; nevertheless, a necessary condition for shakedown can be derived from shakedown theorems in non-associated plasticity (Maier, 1969; de Saxcé and Bousshine, 1998; Ponter, 2016), providing un upper-bound to the shakedown load (Björkman and Klarbring, 1987).

Besides, limit analysis theorems can be conveniently formulated as an optimization problem, in which the objective function, usually represented by the variable load multiplier, is either minimised or maximised with respect to a finite set of unknowns and subjected to problem-specific constraints. In elastic frictional systems, such an approach provides the load multipliers corresponding to the first violation of the stick condition (the so-called stick limit) and to the shakedown condition (the frictional shakedown limit). In the latter case, the optimal distribution of slips represents the unknowns of the problem. Providing an efficient and time-saving approach with respect to cumbersome incremental procedures, various optimisation algorithms developed in the framework of linear and non-linear programming have been proposed (Flicek et al., 2015a; Spagnoli et al., 2017; Figueiredo and Borges, 2020).

The purpose of our work is to present a comprehensive study of shakedown in three-dimensional elastic systems with Coulomb's friction, which received far less attention with respect to plane problems. Indeed, the two-dimensional contact problem is piecewise linear with only backward or forward directions for the frictional slip, whereas the three-dimensional counterpart results in a fully non-linear problem (Cho and Barber, 1999). The aims of this paper are: (i) to analyse the occurrence of frictional limit states in a simple one-node system (Klarbring, 1990) subjected to cyclic loading, and show how the shakedown condition is affected by normal-tangential coupling; (ii) to present a linear programming algorithm which enables a direct computation of stick and shakedown limits in three-dimensional frictional systems; (iii) to compare the previous results with a novel efficient incremental algorithm based on Gauss-Seidel method (Ahn and Barber, 2008). General loading scenarios, including a constant normal component and cyclic tangential loads, in terms of either shear forces or bulk stresses, are applied to multi-node systems. These include the case of a symmetric contact between two square blocks, with equal or different elastic properties, and the problem of an elastic punch on an elastically similar half-space. The final discussion provides an overall view and a critical analyses of the results, with the specific aim of shedding light into the peculiarities of two- and three-dimensional problems.

2. Formulation of the three-dimensional contact problem

We consider a three-dimensional problem in which two elastic bodies $\Omega^{(j)} \in \mathbb{R}^3$, with $j = 1, 2$, are put into contact at a certain period of time $t = [0, T]$, and let $\Gamma^{(j)} = \partial\Omega^{(j)}$ define the boundaries along which suitable conditions are imposed (Klarbring, 1986). We can write $\Gamma^{(j)} = \Gamma_S^{(j)} \cup \Gamma_U^{(j)} \cup \Gamma_C^{(j)}$, with the

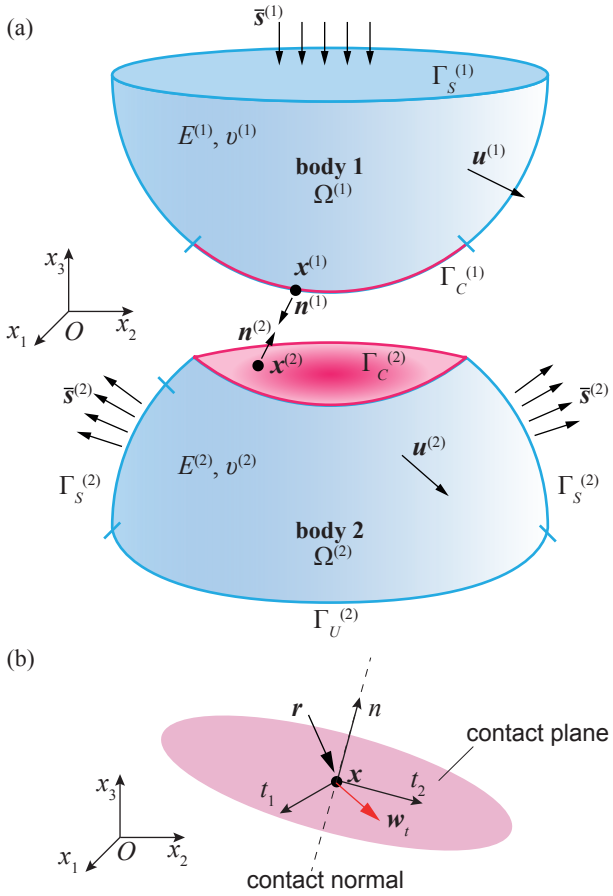

Figure 1. (a) Schematic figure of the three-dimensional contact between two linear elastic bodies, where the red regions represent the conforming contact surfaces. (b) Contact tangential plane at a generic point $\boldsymbol{x}^{(j)} \in \Gamma_C^{(j)}$, with illustration of the general reference system (x_1, x_2, x_3) and the local axes (t_1, t_2, n). 1-col figure

subscripts identifying regions where, respectively, applied tractions, displacements and potential contact events during $[0, T]$ are prescribed. Furthermore, we assume that the contact regions are conforming surfaces, with $\Gamma_C^{(1)} = \Gamma_C^{(2)}$ (Fig. 1).

To introduce the constraints governing the two-body interaction, let us define the outward unit normal vector $\boldsymbol{n}^{(j)}$, the displacement vector $\boldsymbol{u}^{(j)}$ and the stress tensor $\boldsymbol{\sigma}^{(j)}$ for each body. Under the

assumption of conforming contact surfaces, for each point $\boldsymbol{x}^{(1)} \in \Gamma_C^{(1)}$ a corresponding point $\boldsymbol{x}^{(2)} \in \Gamma_C^2$ can be identified, according to the criterium of the nearest point to $\boldsymbol{x}^{(1)}$ on $\Gamma_C^{(2)}$[1]. In a contact point $\boldsymbol{x}^{(j)} \in \Gamma_C^{(j)}$ we can define relative normal and tangential displacements as follows

$$w_n = -[\boldsymbol{u}^{(1)} \cdot \boldsymbol{n}^{(1)} + \boldsymbol{u}^{(2)} \cdot \boldsymbol{n}^{(2)}] \tag{1a}$$

$$\boldsymbol{w}_t = \boldsymbol{u}_t^{(1)} - \boldsymbol{u}_t^{(2)}, \text{ with } \boldsymbol{u}_t^j = \boldsymbol{u}^{(j)} - (\boldsymbol{u}^{(j)} \cdot \boldsymbol{n}^{(j)})\boldsymbol{n}^{(j)} \tag{1b}$$

while contact stresses can be written as

$$r_n = -\boldsymbol{n}^{(j)} \cdot \boldsymbol{\sigma}^{(j)} \boldsymbol{n}^{(j)} \tag{2a}$$

$$\boldsymbol{r}_t = \boldsymbol{\sigma}_t^{(1)} = -\boldsymbol{\sigma}_t^{(2)}, \text{ with } \boldsymbol{\sigma}_t^{(j)} = \boldsymbol{\sigma}^{(j)} \boldsymbol{n}^{(j)} - r_n \boldsymbol{n}^{(j)} \tag{2b}$$

where we have considered the normal component r_n to be positive if compressive; t, n are employed to denote the tangential plane and the normal direction to the contact surface, respectively. Finally, with

[1] As sketched in Fig. 1a, conforming contact surfaces might include the case where a concave surface is in contact with a convex counterpart, subject only to the requirement that nearest points on the two surfaces share the same curvature; such a case would include the limiting one of planar contact where the curvatures tend to zero.

the hypothesis of small displacements, in the contact region we have $\boldsymbol{n}^{(1)} \approx -\boldsymbol{n}^{(2)} \equiv \boldsymbol{n}$ and find

$$\boldsymbol{w} = \boldsymbol{w}_t + w_n \boldsymbol{n}, \qquad \boldsymbol{w}_t \cdot \boldsymbol{n} = 0 \tag{3a}$$

$$\boldsymbol{r} = \boldsymbol{r}_t - r_n \boldsymbol{n}, \qquad \boldsymbol{r}_t \cdot \boldsymbol{n} = 0 \tag{3b}$$

In the present work, we further restrict our attention to complete contacts, that is those in which the contact domain $\Gamma_C^{(j)}$ is known and separation is prevented at all times in $[0, T]$, i.e. (Klarbring et al., 2007)

$$w_n = 0,\ r_n \geq 0 \tag{4}$$

The problem's formulation is completed with the usual balance laws, the constitutive equation for a linear elastic material and prescribed boundary conditions (refer to Klarbring (1986) for a detailed presentation). In particular, the boundary conditions in our problems are taken as

$$\boldsymbol{u}^{(2)} = \bar{\boldsymbol{u}}^{(2)} \quad \text{in}\, \Gamma_U^{(2)},\ \text{for all}\, t \in [0, T] \tag{5a}$$

$$\boldsymbol{\sigma}^{(j)} \boldsymbol{n}^{(j)} = \bar{\boldsymbol{s}}^{(j)} \quad \text{in}\, \Gamma_S^{(j)},\ \text{for all}\, t \in [0, T] \tag{5b}$$

where $\bar{\boldsymbol{u}}^{(2)}$ denote the initial conditions imposed on body two and $\bar{\boldsymbol{s}}^{(j)}$ are external tractions. The loading regime is comprised of a constant part and a time-variable component, which can be expressed by the

resultant of the applied forces as

$$\boldsymbol{F}(t) = \boldsymbol{F}_o + \lambda \boldsymbol{F}_c(t) \tag{6}$$

where λ is a positive load multiplier and the subscripts o and c denote, respectively, the static and cyclic parts of the force vector.

2.1. Coulomb's friction law

To present the mathematical formulation of Coulomb's friction law, we introduce the coefficient of friction f and specify an additional constraint to the previous conditions of Eq. (4), namely

$$\|\boldsymbol{r}_t\| \leq f r_n \tag{7}$$

and

$$\dot{\boldsymbol{w}}_t = -\dot{\gamma}\boldsymbol{r}_t, \quad \text{where} \begin{cases} \dot{\gamma} = 0, & \text{if} \quad \|\boldsymbol{r}_t\| < f r_n \\ \dot{\gamma} \geq 0, & \text{if} \quad \|\boldsymbol{r}_t\| = f r_n \end{cases} \tag{8}$$

where $\dot{\gamma}$ is a non-negative multiplier rate and $\dot{\boldsymbol{w}}_t$ is the time derivative of the tangential contact displacement, that is, the slip rate.

Equation (7) requires the magnitude of the tangential stress vector not to exceed the contact pressure multiplied by the coefficient of friction. Namely, the contact stresses must belong to the so-called Coulomb cone of friction, whose axis is coincident with the positive axis of the normal contact reaction r_n, with the apex lying at $r_n = 0$ (Fig. 2). On the other hand, Eq. (8) defines the limit condition:

it specifies that the tangential slip $\dot{\boldsymbol{w}}_t$ is identically zero when the tangential reaction $\boldsymbol{r}_t$ is less than the Coulomb limit, while when it is non-zero, its direction opposes the frictional reaction $\boldsymbol{r}_t$, whose magnitude is then equal to $f\boldsymbol{r}_n$. Coulomb's law can also be presented in a rate formulation typical of elasto-plastic constitutive laws (Michalowski and Mroz, 1978)

$$\phi(\boldsymbol{r}_t, r_n) = \|\boldsymbol{r}_t\| - f r_n \leq 0 \tag{9a}$$

$$\dot{\boldsymbol{w}}_t = -\dot{\gamma}\frac{\boldsymbol{r}_t}{\|\boldsymbol{r}_t\|} \tag{9b}$$

$$\dot{\gamma}\phi = 0, \quad \dot{\gamma} \geq 0 \tag{9c}$$

where ϕ is the so-called slip function and Eq. (9b) is the flow rule. It appears evident that Coulomb's law is non-associated, since the direction of the slip rate is defined by the tangential component of the contact reaction. More correctly, we can say that the normality rule is satisfied by the slip rate and the contact reactions in the tangential plane, but the set of admissible forces depends on the present value of r_n. This also means that, whenever we can consider the normal reaction independent on slip, that is to say, when the normal reaction is determined by the sole equilibrium with external loads, the normality rule applies (Michalowski and Mroz, 1978). This is the concept behind the extension of limit analyses theorems to frictional problems (Klarbring et al., 2007, 2017).

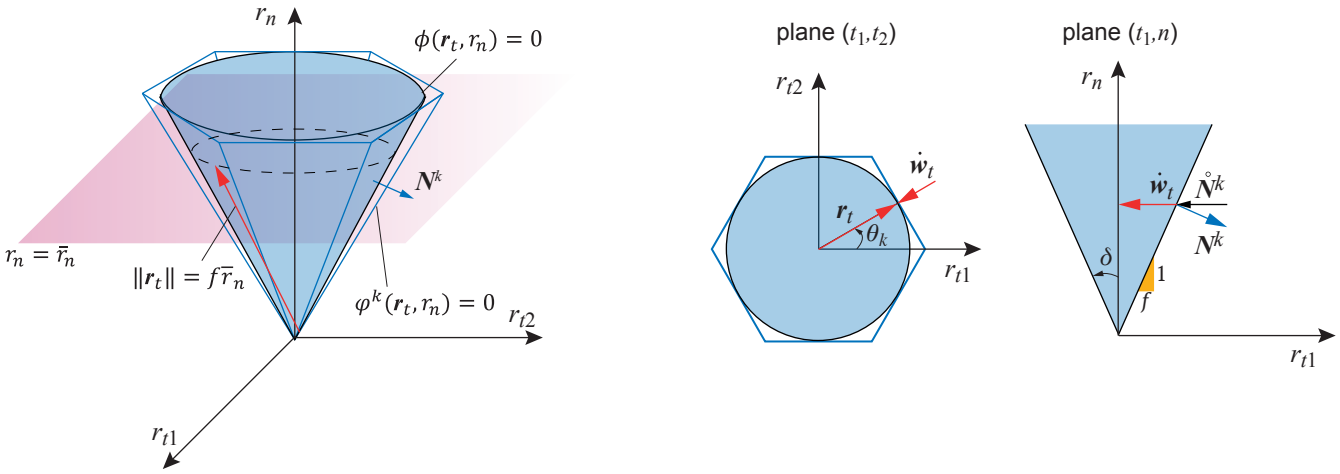

Figure 2. Coulomb's friction cone in three-dimensions, with $r_n > 0$ when compressive. The red arrow represents the limit state in a generic point, i.e. when $\|\boldsymbol{r}_t\| = f\bar{r}_n$. Projections on the planes (t_1, t_2) and (t_1, n), displaying the slip vector $\dot{\boldsymbol{w}}_t$, are shown. The latter, which also corresponds to Coulomb's cone in two-dimensional problems, shows the unit normal vector along the slip direction $\mathring{\boldsymbol{N}}^k$. A piecewise linearisation of Coulomb's friction cone with a circumscribed polyhedron, where each face is identified by the normal vector $\boldsymbol{N}^k$, is introduced for later use in the linear programming problem of Sect. 3. 2-col figure

2.2. Discretisation and condensation

For later use, we introduce a discretisation of the problem illustrated in Fig. 1a (for instance, by using the finite element method). Let us assume that one of the conforming contact surfaces $\Gamma_C^{(j)}$ comprises N nodes in potential contact and collect relative displacements and contact reactions in ordered arrays as follows (refer to the local reference system as shown in Fig. 1b)

$$\boldsymbol{w} = [\boldsymbol{w}_{t1}\ \boldsymbol{w}_{t2}\ \boldsymbol{w}_n]^T, \quad \boldsymbol{r} = [\boldsymbol{r}_{t1}\ \boldsymbol{r}_{t2}\ \boldsymbol{r}_n]^T \tag{10}$$

By a standard static condensation procedure (Thaitirarot et al., 2014), we can eliminate the dis-

placements associated with the internal nodes and write the reaction forces in the form

$$\boldsymbol{r}(t) = \boldsymbol{r}^e(t) + \boldsymbol{\kappa}\boldsymbol{w}(t) \tag{11}$$

where $\boldsymbol{\kappa}$ is a reduced contact stiffness matrix that is symmetric and positive semi-definite. In Eq. (11), $r_e(t)$ are the generally time-varying reaction forces that would be generated at the contact nodes by external loads if displacements at these nodes were constrained to be zero. The remaining term represents instead the modification to contact reactions resulting from slips. The solution of the discrete contact problem consists in finding the time evolution of $\boldsymbol{w} = \boldsymbol{w}(t)$ and $\boldsymbol{r} = \boldsymbol{r}(t)$ for the given history of external loading, Eq. (6).

2.3. Frictional shakedown

Upon the application of the external loads in Eq. (6), it is assumed that the system response is initially elastic and contact reactions follow an analogous time evolution, so that

$$\boldsymbol{r}^e(t) = \boldsymbol{r}^e_o + \lambda \boldsymbol{r}^e_c(t) \tag{12}$$

After the limit condition of Coulomb's friction law, Eqs. (7) and (9a), is achieved, frictional slips develop at the contact interface according to the slip rule, Eqs. (8) and (9b). The system is further submitted to cyclic loading with period T_c, such that the initial transient stage is followed by a cyclic stage. A steady state is attained when, at a certain time instant $t > 0$, the system response becomes a

periodic function with period equal to that of the external loading. In terms of contact reactions, such a condition corresponds to $\boldsymbol{r}(t) = \boldsymbol{r}(t+T_c)$, where these terms now also include an irreversible term due to frictional slips. The system behaviour in the steady state depends on the evolution of slips: frictional shakedown occurs when slips are confined to the transient stage while in the steady state the system recovers an elastic response, with no energy dissipation. Mathematically, this corresponds to $\dot{\boldsymbol{w}}_t = \boldsymbol{0}$ (Klarbring et al., 2017). The problem we are interested in is assessing the shakedown occurrence for a given loading history. In other terms, we shall find the multiplier of variable loads λ, usually defined as the shakedown limit, which discriminates between non-dissipative and dissipative states.

2.4. Contact coupling

The reduced stiffness matrix $\boldsymbol{\kappa}$ in Eq. (11) can be partitioned as follows

$$\boldsymbol{\kappa} = \begin{bmatrix} \boldsymbol{\kappa}_{tt} & (\boldsymbol{\kappa}_{nt})^T \\ \boldsymbol{\kappa}_{nt} & \boldsymbol{\kappa}_{nn} \end{bmatrix} \tag{13}$$

with

$$\boldsymbol{\kappa}_{tt} = \begin{bmatrix} \boldsymbol{\kappa}_{t_1t_1} & (\boldsymbol{\kappa}_{t_2t_1})^T \\ \boldsymbol{\kappa}_{t_2t_1} & \boldsymbol{\kappa}_{t_2t_2} \end{bmatrix}, \quad \boldsymbol{\kappa}_{nt} = \begin{bmatrix} \boldsymbol{\kappa}_{nt_1} & \boldsymbol{\kappa}_{nt_2} \end{bmatrix} \tag{14}$$

where the main sub-matrices in Eq. (13) correspond to the following force-displacement relationships: tangential-tangential $\boldsymbol{\kappa}_{tt}$, normal-tangential $\boldsymbol{\kappa}_{nt}$, normal-normal $\boldsymbol{\kappa}_{nn}$.

The term $\boldsymbol{\kappa}_{nt}$ has traditionally been associated to contact coupling; more specifically, it quantifies the

normal contact forces that are generated by tangential slip displacements (Flicek et al., 2017) and the necessary and sufficient condition for an uncoupled contact is that $\boldsymbol{\kappa}_{nt} = \mathbf{0}$. In more detail, Flicek et al. (2017) proposed a metrics to estimate coupling in an aggregate sense, by looking at some properties of contact stiffness submatrices. An alternative way to quantify coupling in a point-wise sense is by defining a coefficient ranging from 0 to 1 (where zero means no coupling), as shown for instance in Klarbring et al. (2007), where the maximum normal reaction force resulting from the set of all possible tangential displacement distributions is considered. Peculiar to three-dimensional problems is coupling between the tangential directions on the contact plane, controlled by the second level sub-matrix $\boldsymbol{\kappa}_{t_2t_1}$. The effect of each term of the reduced stiffness matrix will be trivially explored on a single node system in Sect. 4. In multi-node systems (Sect. 5), normal-tangential coupling might arise from two sources, namely material mismatch and domain mismatch. The former has been known for long in contact mechanics, as it is related to the separation between tangential (normal) relative displacements and distributed normal (tangential) tractions in the half-plane problem by Flamant (Barber, 2018). Domain mismatch arises instead because the elasticity solutions are in different elastic domains due to the finite size of the contacting bodies (Churchman and Hills, 2006). In practice, the only real case of perfect uncoupling is between two elastically similar and symmetric bodies, as it will be shown in Sect. 5.1. A thorough discussion of coupling is beyond the scope of our work; however, we shall spend a few more words on its role with respect to the occurrence of shakedown in the next Section, and leave the interested reader to the recent work by Flicek et al. (2017) on two-dimensional systems.

3. The linear programming problem

The relevant problem of assessing the occurrence of shakedown can be conveniently formulated in the framework of mathematical programming, taking advantage of the shakedown theorems for non-associated flow rules (Maier, 1969; Klarbring, 1986). Following the classical arguments of limit analysis, Klarbring et al. (2007) have proved a static theorem which provides a lower bound to the shakedown limit whenever $\boldsymbol{\kappa}_{nt} = \mathbf{0}$, based on the existence of a safe residual displacement distribution. Indeed, this is the only case in which Coulomb's flow rule becomes associated (see Sect. 2.1). In the general scenario, there almost always exists a range of load multipliers λ for which the response of the system in the steady state is affected by initial conditions. In this work, we shall always assume a null initial slip distribution, i.e. $\boldsymbol{w}(t = 0) = \mathbf{0}$. We here introduce the definition of limit load multipliers that will be employed throughout the remaining part of our work. The information is summarised in the graphical representation of Fig. 3.

- stick limit λ_0: the load multiplier corresponding to the first violation of the stick condition;
- shakedown lower bound λ_1: the load multiplier below which frictional shakedown is guaranteed;
- shakedown upper bound λ_2: the load multiplier above which frictional shakedown is impossible: that is, any state corresponding to $\lambda > \lambda_2$ is energy dissipating.

Notice that, if such limits exist, $\lambda_0 \leq \lambda_1 \leq \lambda_2$ while $\lambda_2 = \lambda_1$ in uncoupled contacts only. We also introduce here the dissipative load multiplier λ_D, which in the incremental analyses discriminates

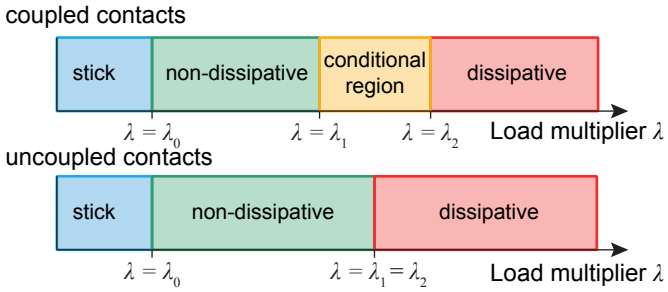

Figure 3. Sketch illustrating the possible responses of coupled and uncoupled contacts in the steady state, in terms of the multiplier λ of cyclic loads. In the conditional yellow region, the system response can be either energy dissipative or non-dissipative depending on initial conditions. 1-col figure

energy dissipative from non-dissipative simulations for given initial conditions (with $\lambda_1 \leq \lambda_D \leq \lambda_2$). Interestingly, a programming method for the limit λ_D based on the linear matching method, has been proposed by Ponter (2016) for two-dimensional linear elastic bodies in contact with planar rigid surfaces. Based on the necessary condition for shakedown in non-associated plasticity, Björkman and Klarbring (1987) devised a method to compute the shakedown upper bound λ_2 for a generic two-dimensional frictional system, with the sole requirement of the loading domain to be convex and its limits known. We shall here extend their approach to three-dimensional systems.

3.1. Optimisation algorithm

Differently from the two-dimensional case, in three dimensions the frictional contact problem is fully non-linear, since the admissible domain for the slip vector is the whole projection of Coulomb's cone on the contact plane. Following Klarbring (1986), we consider a piecewise linearisation of the slip surface by means of a polyhedron (Fig. 2) and identify its faces with a unit normal vector $\boldsymbol{N}^k$, which is defined

by

$$\boldsymbol{N}^k = \cos\delta \, [\cos\theta^k, \sin\theta^k, -\tan\delta]^T \tag{15}$$

where θ^k is the anti-clockwise angle formed by the normal to the k-th face and $\tan\delta = f$ (the minus in Eq. (15) is due to the contact normal reactions being positive when compressive). Then the slip function in Eq. (9a) is replaced by a set of functions written as

$$\varphi^k = \boldsymbol{N}^{kT}\boldsymbol{r} \leq 0, \qquad k = 1, ..., K \tag{16}$$

where K is the total number of faces of the polyhedron. In two-dimensional problems, we have $K = 2$, corresponding to the following slip functions of backward and forward slip, respectively (Björkman and Klarbring, 1987)

$$\varphi^1 = -fr_n + r_t, \qquad \varphi^2 = -fr_n - r_t. \tag{17}$$

Following the linearisation, the flow rule in Eq. (9b) is written as

$$\dot{\boldsymbol{w}} = \sum_{k=1}^{K} \mathring{\boldsymbol{N}}^k \dot{\gamma}^k \tag{18}$$

where $\mathring{\boldsymbol{N}}^k$ identifies the inward unit normal vector to the face of the polyhedron in the contact plane,

where the normality rule applies (Fig. 2), and is given by

$$\mathring{\boldsymbol{N}}^k = [-\cos\theta^k, -\sin\theta^k, 0]^T \tag{19}$$

Inserting the expression of the contact reactions given by Eq. (11) in Eq. (16), and replacing the slips with the form of Eq. (18), the set of slip functions is substituted by

$$\Phi = \boldsymbol{N}^T \boldsymbol{r}^e(t) + \boldsymbol{N}^T \boldsymbol{\kappa} \mathring{\boldsymbol{N}} \boldsymbol{\gamma} \leq 0 \tag{20}$$

where we have assembled the non-negative multiplier γ^k in an array, the normal vectors $\boldsymbol{N}^k$ and $\mathring{\boldsymbol{N}}^k$ in block diagonal matrices for the whole polyhedron and we have removed the dots from the slip rate of Eq. (18).

The last step to take is removing the time dependence from Eq. (20), which can be done because of the hypothesis of convex load domain. Following Björkman and Klarbring (1987), we can replace the effective history with an equivalent cycle of loading passing uniquely for the extreme values of loads. Mathematically, this is achieved by computing the maximum of the projection of $\boldsymbol{r}_c^e(t)$ on the normal vector with respect to the V vertices of the load domain, that is

$$\boldsymbol{M} = \max_v \left(\boldsymbol{N}^T \boldsymbol{r}_c^e(t_v) \right), \quad v = 1, ..., V \tag{21}$$

Finally, the shakedown upper bound λ_2 is obtained from the following linear optimisation problem

$$\lambda_2 = \max_{\lambda,\boldsymbol{\gamma}} \lambda \qquad \text{subject to :} \tag{22}$$

$$(I)\ \lambda \boldsymbol{M} + \boldsymbol{N}^T \boldsymbol{\kappa} \mathring{\boldsymbol{N}} \boldsymbol{\gamma} \leq -\boldsymbol{N}^T \boldsymbol{r}_o^e$$

$$(II)\quad \boldsymbol{\gamma} \geq \boldsymbol{0}$$

$$(III)\quad \lambda \geq 0$$

where the variable load multiplier λ is maximised, subjected to the linear constraints of Coulomb's law, and the vector of optimal slips $\boldsymbol{w}_{\text{op}} = \mathring{\boldsymbol{N}} \boldsymbol{\gamma}$ is provided. Notice that the stick limit λ_0 is also computed with this algorithm by taking $\boldsymbol{\gamma} = \boldsymbol{0}$ in Eq. (22).

4. Single-node frictional system

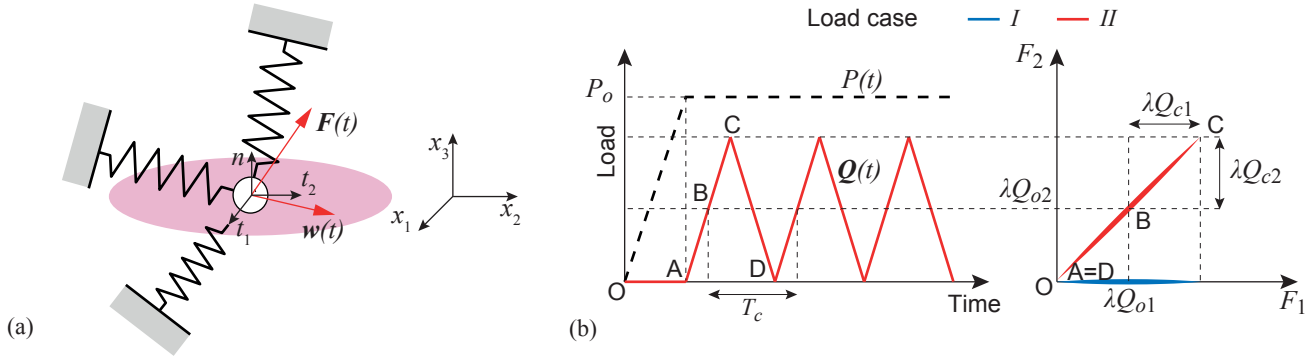

Figure 4. (a) Sketch of the three-dimensional single-node frictional system, with the contact plane aligned to the coordinates x_1, x_2. (b) Loading scheme considered in this work, showing the time evolution with cycles of length T_c and domain in the plane of the tangential component $\boldsymbol{Q}(t)$. 2-col figure

We here consider a single node three-dimensional system, which is an extension of the model discussed in Klarbring (1990) with three degrees of freedom. An illustrative sketch is provided in Fig. 4a, where it is shown that the contact plane is aligned with the plane (x_1, x_2), such that the global and local reference directions coincide. The notation employed in the following therefore adopts the global indices. Following the work by Cho and Barber (1998, 1999), we employ this elementary problem in order to explore the response of a three-dimensional system to cyclic loading and shed light on how frictional shakedown is affected by coupling. The stick and shakedown limits are firstly obtained from the linear optimisation algorithm presented in Sect. 3. Then, we employ a modified version of the Gauss-Seidel algorithm described by Ahn and Barber (2008) to perform incremental analyses and compare the results from optimisation (Beccarelli, 2020). Finally, we show how the steady state behaviour can be predicted by simple geometric reasoning derived from the imposition of the frictional constraints.

The quasi-static solution of the frictional contact problem is described by the following equilibrium equations (Cho and Barber, 1999)

$$\boldsymbol{\kappa} \boldsymbol{w} = \boldsymbol{F} + \boldsymbol{r} \tag{23}$$

where the stiffness matrix $\boldsymbol{\kappa}$ has six coefficients derived from a system of three linear springs (Fig. 4a). However, the coordinate system in the tangential plane can be chosen to have κ_{31} equal to zero, so that

we can write

$$\boldsymbol{\kappa} = \begin{bmatrix} \kappa_{11} & \kappa_{21} & 0 \\ \kappa_{21} & \kappa_{22} & \kappa_{32} \\ 0 & \kappa_{32} & \kappa_{33} \end{bmatrix} \tag{24}$$

Under the constraints of the frictional contact problem, as described in Sect. 2, the system admits three possible states:

i) *stick*, when $\dot{\boldsymbol{w}}_t = 0$, $w_n = 0$ and $r_n > 0$, with the frictional constraint $\|\boldsymbol{r}_t\| < f r_n$;

ii) *slip*, when $w_n = 0$, $r_n > 0$ and $\dot{\boldsymbol{w}}_t \neq 0$;

iii) *separation*, when $w_n > 0$ and $\boldsymbol{r} = 0$.

Following Cho and Barber (1999), we shall consider $f < f_c$, where f_c is a critical coefficient of friction needed to ensure uniqueness of the quasi-static solution, defined by

$$f_c = \frac{d_3}{\sqrt{d_1^2 + d_2^2}} \quad \text{and} \quad d_i = e_{ijk}\kappa_{j1}\kappa_{k2} \tag{25}$$

are the components of the unit normal to the separation plane in the space of external forces F_i (e_{ijk} is the permutation tensor and summation convention for repeated indices applies)(Cho and Barber, 1999).

In the following, we analyse the response of the system subjected to the loading history defined in

Eq. (6). Specifically, we take

$$\boldsymbol{F}(t) = \left\{ \begin{array}{c} F_1(t) \\ F_2(t) \\ F_3(t) \end{array} \right\} = \left\{ \begin{array}{c} \boldsymbol{Q}(t) \\ P(t) \end{array} \right\} = - \left\{ \begin{array}{c} \lambda Q_{o1} \\ \lambda Q_{o2} \\ P_o \end{array} \right\} - \left\{ \begin{array}{c} \lambda Q_{c1} \\ \lambda Q_{c2} \\ 0 \end{array} \right\} f(t) \tag{26}$$

where $f(t) \in [-1, +1]$. Notice that the load factor λ here multiplies both the mean value and the amplitude of tangential loads. The normal component $P(t)$ is increased from zero and kept constant at P_o, while the tangential component $\boldsymbol{Q}(t)$ is applied monotonically (point A in Fig. 4b) and then oscillates around its mean value $\lambda \boldsymbol{Q}_o$ (point B) with amplitude $\lambda \boldsymbol{Q}_c$. Two loading cases are considered, as illustrated in Fig. 4b:

1. load case I, where F_1 is applied (with $Q_{o1} = Q_{c1} = P_o$) while $F_2 = 0$;

2. load case II, where both tangential components are applied in phase (with $Q_{o1} = Q_{c1} = P_o$ and $Q_{o2} = Q_{c2} = P_o$).

For what has been said in Sect. 3, the full loading history needs to be considered in incremental analyses, while the extremes only (represented by C and D in Fig. 4b) are required in the optimisation.

The stiffness matrix of the one-node system, Eq. (24), has been chosen to explore three different coupling scenarios:

a. full coupling, with $\kappa_{11} = 1, \kappa_{21} = 1, \kappa_{22} = 6, \kappa_{32} = -5, \kappa_{33} = 7$. We find

$$\boldsymbol{d} = [-1/\sqrt{3},\ 1/\sqrt{3},\ 1/\sqrt{3}]^T \text{and } f_c = 1/\sqrt{2};$$

b. no tangential coupling, with $\kappa_{11} = 1, \kappa_{21} = 0, \kappa_{22} = 6, \kappa_{32} = -5, \kappa_{33} = 7$. We find

$$\boldsymbol{d} = [0,\ 0.6402,\ 0.7682]^T \text{and } f_c = 1.2;$$

c. no normal-tangential coupling, with $\kappa_{11} = 1, \kappa_{21} = 1, \kappa_{22} = 6, \kappa_{32} = 0, \kappa_{33} = 7$. We find

$$\boldsymbol{d} = [0,\ 0,\ 1]^T \text{and } f_c \to \infty.$$

4.1. Stick and shakedown limits

The linear optimisation algorithm is employed to compute the load multipliers corresponding to the stick limit λ_0 and the shakedown upper bound λ_2. The optimisation curves are then compared with results deriving from Gauss-Seidel incremental analyses. Briefly, this algorithm assumes that the state of a contact node, correctly determined at the instant of time t, continues to apply even following a finite temporal increase Δt. In the ensuing incremental analyses, suitable time steps are adopted on the base of a preliminary convergence study, comprised between $\Delta t = T_c/80$ for the single-node system and $\Delta t = T_c/400$ for multi-node frictional systems of Sect. 5 below. Initially, a state of stick is assumed;

then, at the generic time step t_j, reactions r_{t1}, r_{t2} and displacements w_{t1}, w_{t2} are computed. At this point, the inequalities of Coulomb's friction law are checked to verify the state of the node, i.e. stick, slip or separation (although the latter is not considered in the present paper concerning complete contacts). If the verification is positive, the previous status of the node is provisionally confirmed. Otherwise, the status is updated according to the type of violation and the relative displacements are calculated. In Sect. 5, where we consider multi-node systems, this procedure will be performed node-by-node; when the state is checked on the selected node, the quantities related to all the other nodes take the value calculated at the end of the previous instant t_{j-1} and the procedure is iterated until the real state corresponding to each node of the contact interface is identified. More details about the Gauss-Seidel procedure and its implementation in three-dimensional multi-node systems can be found in Beccarelli (2020). In order to distinguish the system response at the steady state, the dissipated energy per cycle is computed according to (Flicek et al., 2015a)

$$W_l = -\sum_{i=1}^{N} \oint \left(r_{t1}^{(i)} \dot{w}_{t1}^{(i)}(t) + r_{t2}^{(i)} \dot{w}_{t2}^{(i)}(t) \right) \mathrm{d}t \tag{27}$$

where the closed loop integral refers to the l-th cycle, while sum is extended to all the N contact nodes (in the single-node problem, we have $N = 1$). The system is considered in a condition of shakedown when the energy dissipated in the last cycle is less than a sufficiently small tolerance. Notice that the algorithm does not use a normalised definition of the dissipated energy; instead, the appropriate value of tolerance is set with a trial-and-error procedure. This because we have found that, depending on

the problem, the threshold value changes. Moreover, we have noticed that the cyclic response stabilizes after a few cycles and a threshold value based only on the ratio of dissipation in successive cycles does not seem to be applicable.

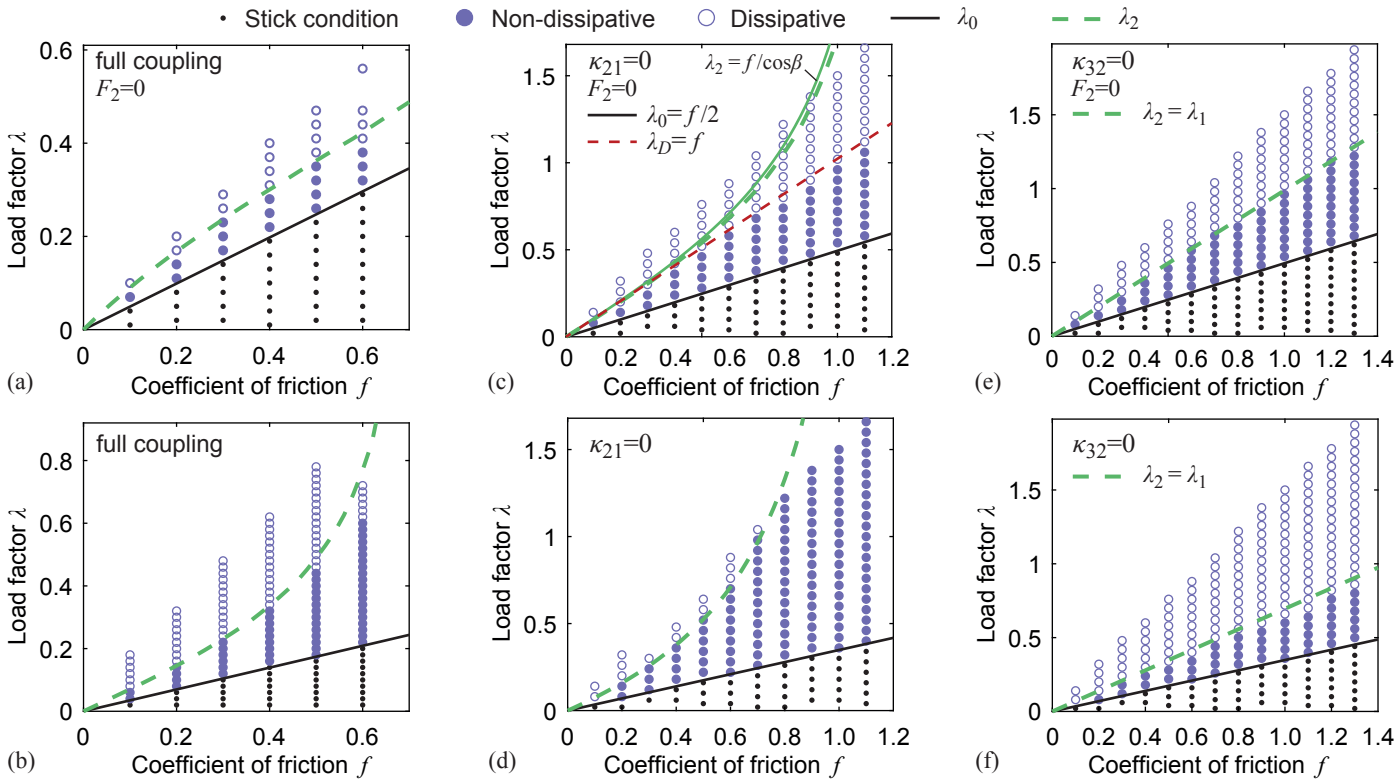

Figure 5. Stick and shakedown load multipliers λ_0 and λ_2 obtained from linear optimisation and comparison with results from incremental analyses using the Gauss-Seidel algorithm. Both load cases and different coupling scenarios are displayed: (a-b) full coupling, (c-d) no tangential coupling ($\kappa_{21} = 0$), (e-f) no normal-tangential coupling ($\kappa_{32} = 0$). In (c), analytical values of the limits are derived according to the calculations described in Sect. 4.2, with λ_D representing the limit between dissipative and non-dissipative simulations (for the meaning of angle β refer to Fig. 7). 2-col figure

Results of the optimisation algorithm and incremental analyses are summarised in Fig. 5 as a function of the friction coefficient $f < f_c$, for the two load cases and three coupling scenarios previously

described. The accuracy of the optimisation is affected by the total number of faces of the polyhedron K and preliminary analyses suggested that $K \geq 36$ is enough to obtain full convergent solutions. We at once observe that the normal-tangential uncoupled situation, when $\kappa_{32} = 0$, is the only one showing perfect agreement between incremental and optimisation results (Fig. 5e,f) in the whole spectrum of friction coefficients. Indeed, the lower and upper bounds to the shakedown load λ_1 and λ_2 coincide without a conditional region; minor discrepancies might depend on the numerical threshold separating dissipative and non-dissipative behaviour. On the contrary, the other scenarios suggest that dissipative states (hollow circles in figures) might exist below the shakedown limit λ_2, which indeed represents by definition the limit above which shakedown can never occur. We might draw a tentative curve $\lambda = \lambda_{\mathrm{D}}$ characterising the limit that discriminates dissipative and non-dissipative behaviour (that is, connecting the top row of filled circles); such a curve would always lie below λ_2. However, since our analyses have in no way explored the conditional region existing in coupled contacts (in all incremental analyses we have assumed null initial slips), it might well be that analyses with different initial conditions result in dissipative situations even for lower loads (Flicek et al., 2017).

4.2. Evolution of slips

The main use of incremental analyses is to gain an insight into the evolution of the frictional contact under loading. From the previous simulations, we have selected an intermediate value of friction $f = 0.5$ and extracted frictional slips throughout the whole loading history. Results are summarised in Fig. 6, for a load multiplier $\lambda = \lambda_2$ and $\lambda = 1.2\lambda_2$. Notice that λ_2 is almost coincident with λ_D for $f = 0.5$, so

that in practice simulations with $\lambda = \lambda_2$ are representative of a situation of shakedown. Slips are shown in the dimensionless form $\tilde{w}_m = w_m \kappa_{11}/P_o$ with $m = 1, 2$. All incremental analyses were stopped after three complete loading cycles because we have found that the system had already entered the steady state.

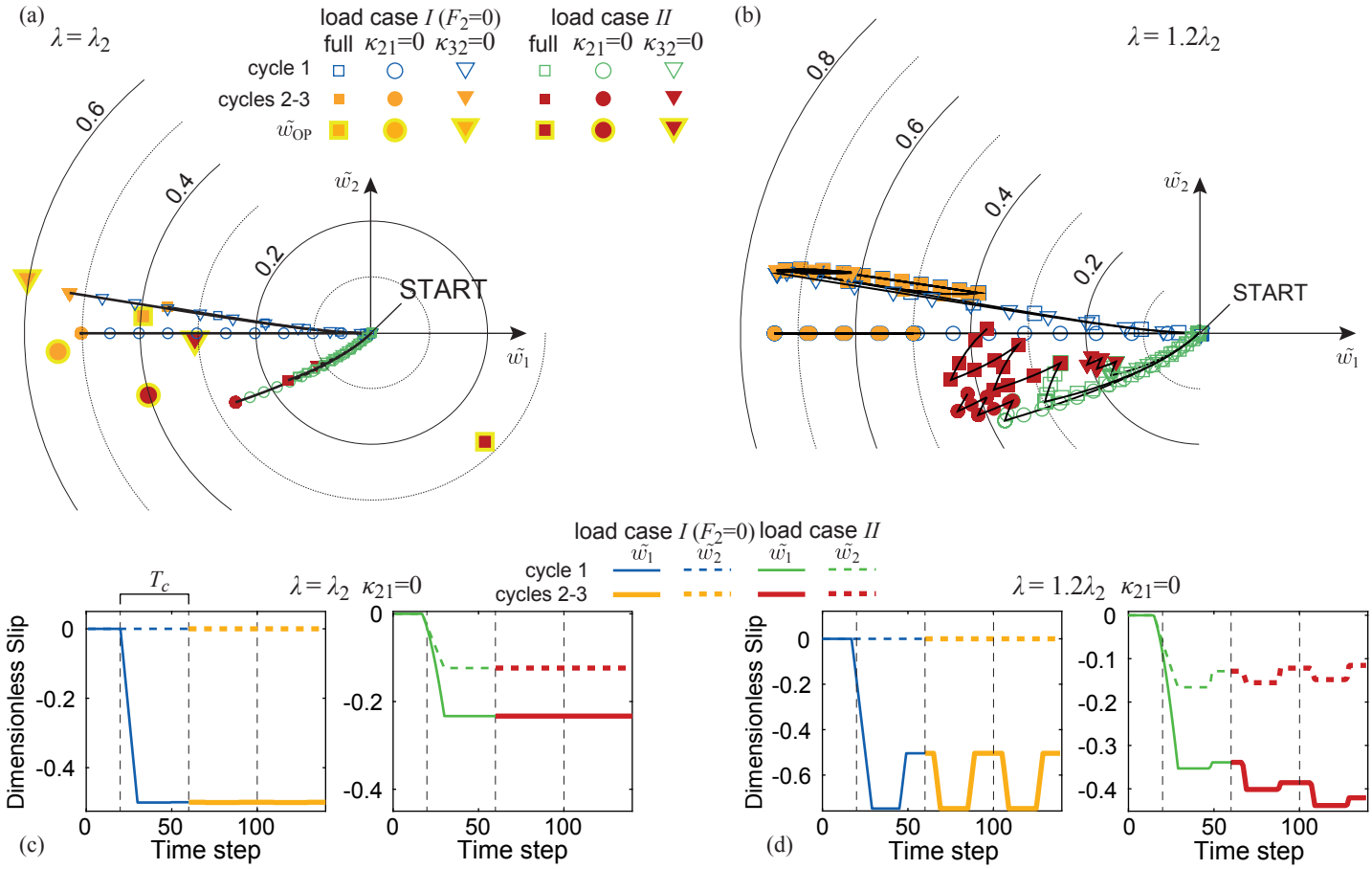

Figure 6. Slip paths in the single-node frictional system, shown on the contact plane for $f = 0.5$, when (a) $\lambda = \lambda_2$ (shakedown) and (b) $\lambda = 1.2\lambda_2$ (energy dissipative response). In (a), highlighted dots are related to the optimal slips $\tilde{\boldsymbol{w}}_{\text{op}}$. (c-d) Corresponding time evolution of slips obtained from Gauss-Seidel analyses, for the case of no tangential coupling ($\kappa_{21} = 0$). Values are shown in dimensionless form; symbols and colours are differentiated between the first and subsequent load cycles of amplitude T_c. 2-col figure

Maps in Fig. 6a,b display the trajectories followed by the single node on the contact plane during the whole loading history, conveying a far more complex picture than the backward or forward slip of plane contact problems. In load case I, Eq. (26) with $F_2 = 0$, the tangential force is applied along x_1 only, hence the loading scheme is two-dimensional: however, slips are developed in both directions, with the only exception in the scenario without tangential coupling (orange circles in figures). To further stress the difference between dissipative and non-dissipative situations we have plotted the time evolution of the slip components in Fig. 6c,d, for the case $\kappa_{21} = 0$. Shaken down simulations (Fig. 6c) display a constant part after the initial transient state in which slips are developed; on the contrary, the steady state response in dissipative situations ($\lambda = 1.2\lambda_2$) appears different depending on the load case. Our analyses suggest that for load case I the node experiences cyclic slip, highlighted by the saw-tooth pattern in Fig. 6d. On the contrary, for load case II, Eq. (26) with $F_1 = F_2 \neq 0$, slips are cumulated, resulting in the so-called ratchetting, at least within the three cycles considered. Optimal slips $\tilde{\boldsymbol{w}}_{\text{op}}$ computed from linear optimisation for $\lambda = \lambda_2$ are superposed to the slip trajectories of Fig. 6a. There is good agreement in terms of magnitude with the slips obtained from incremental analyses, although with some differences. This should not surprise, since the Gauss-Seidel algorithm follows the complete evolution of the frictional system whereas optimal slips are the distribution that maximises the amplitude of cyclic loads without breaking the frictional constraints of the linear programming problem. As discussed in Sect. 3, the curve $\lambda = \lambda_{\text{D}}$ would always lie below λ_2; in turn, we shall expect the optimal slip magnitude to be larger than the real one. We are able to provide an explanation of this through

simple analytical computations.

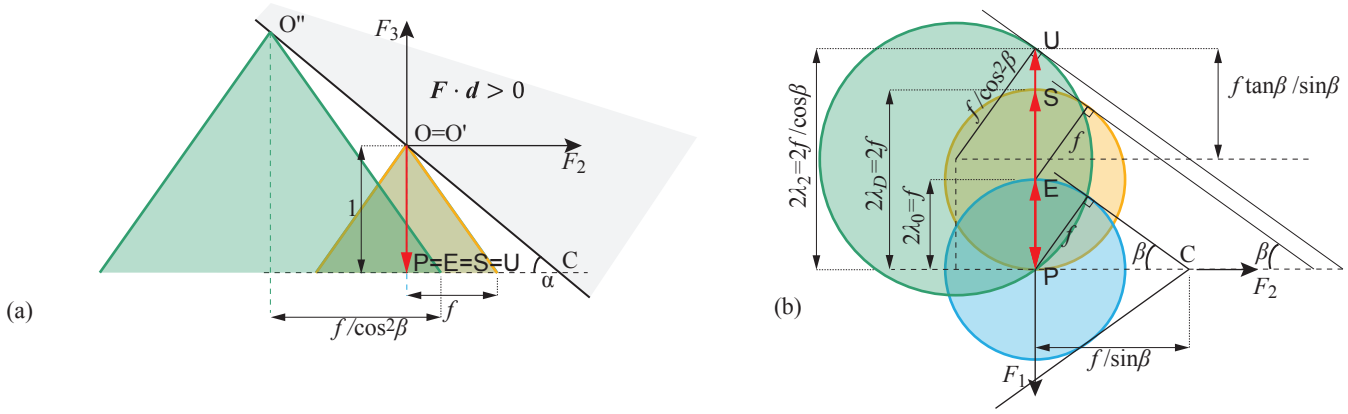

Figure 7. Illustration of the single-node system evolution in the space of external forces F_i, for no tangential coupling and load case I ($F_2 = 0$). (a) Plane F_2, F_3 showing the projection of the separation surface with unit normal $\boldsymbol{d} = [0,\ 0.6402,\ 0.7682]^T$. (b) Tangential plane $F_3 = -P_0 = -1$. The relevant points are related to: P, normal loading only; E, stick limit $\lambda = \lambda_0$; S, dissipative limit $\lambda = \lambda_D$; U, shakedown upper bound $\lambda = \lambda_2$. 2-col figure

Let us again focus on the scenario without tangential coupling ($\kappa_{21} = 0$). In this simple single-node system, we can derive both the limits λ_2 and λ_D analytically and provide an explanation to the fact that the optimal slip array has a non-zero component along the x_2 direction, in contrast to the predictions of Gauss-Seidel results (orange circles in Fig. 6a). Let us consider the space defined by the components of the external force vector F_1, F_2, F_3. As previously mentioned, the condition of separation $\boldsymbol{F}\cdot\boldsymbol{d} > 0$ is represented by a plane passing through the origin $\boldsymbol{F} = \boldsymbol{0}$, with unit normal $\boldsymbol{d}$ (Klarbring et al., 2007). When there is no tangential coupling the unit normal $\boldsymbol{d}$ has a null component in the F_1 direction, so that if we consider the vertical plane F_2, F_3 its projection is represented by a line, whose slope is $\tan\alpha = d_2/d_3$ (Fig. 7a). Incidentally, note that in the case of no normal-tangential coupling the unit normal would

be parallel to the axis F_3. In the tangential plane $F_3 = -P_o$ the diameter of Coulomb's circle is equal to $2fP_o$, while the tangent lines are inclined of an angle $\beta = \arcsin(fd_2/d_3)$ (Fig. 7b). Such an angle is defined by the line belonging to the plane $F_3 = -P_o$, passing through point C and tangent to the circle centred in O. In order to prevent separation, the vertex of any cone has to lie on the separation plane. Initially, the system is brought to point P upon application of normal loading only (according to the sign convention, $F_3 < 0$). Considering load case I, tangential loading is then applied in direction x_1 and the stick limit is encountered on the border of the blue circle centred in O (point E), when $\lambda = \lambda_0 = f/2$. Since $F_2 = 0$ and $w_2 = 0$ at any stage due to the lack of coupling between the tangential directions, we can only have vertical shifts of the cone circles in Fig. 7b as the load multiplier λ is increased. Moreover, for the initial assumption of $\kappa_{31} = 0$ in Eq. (24), the radius cannot increase because there is no coupling between tangential slip w_1 and normal force F_3. Hence, further loading requires the circle to shift to a new one in the tangential plane (yellow circle centred in E), whose border represents the limit $\lambda = \lambda_D = f$ (point S). However, the optimisation shows that there exists an upper limit λ_2 which is larger than the multiplier λ_D, but it can be reached only under specific conditions, namely, the existence of $w_2 \neq 0$, as found in Fig. 6a. From geometrical considerations, we find $\lambda_2 = f/\cos\beta$ (point U); any further increase would not be admissible, since the circle of radius $f/\cos^2\beta$ is the largest passing through the initial point P and tangent to a line inclined of β. The analytical values of load multipliers here computed are illustrated in Fig. 5c, showing a perfect matching with the results of optimisation.

5. Multi-node frictional systems

We now move on to considering multi-node systems, in order to show the potential of the proposed numerical tools to be applied to various geometries. Each of the following examples has been discretised by means of the finite element method with 8-node linear brick elements. The mesh adopted in the FE models is characterized by a uniform spacing of the nodes, with a one-to-one correspondence between boundary nodes on the contacting bodies. Plane models of the corresponding two-dimensional examples have also been generated, with 4-node plane strain elements, keeping the mesh consistent. With respect to the mesh size, we have verified that its refinement along the contact surface is sufficient to ensure good precision in stress approximation, particularly in contacts involving stress concentrations, and convergence in the inner contact region. However, numerical convergence was not rigorously verified as this would have implied a prohibitive computational cost. Upon the application of static condensation by Thaitirarot et al. (2014), see Sect. 2.2, each problem is reduced to the sole contact degrees of freedom, whose number is the same for all the examples provided. The loading history is described by Eq. (26) and illustrated in Fig. 4b; specifically, for each geometry we have considered load case I, when only the component along x_1 is considered ($F_2 = 0$), and load case II, when cyclic loads are applied simultaneously along both the tangential directions x_1, x_2. Each example has been analysed with the optimisation algorithm described in Sect. 3, where Coulomb's cone is linearised by means a polyhedron with $K = 12$ faces (see Fig. 2), and employing incremental analyses with the Gauss-Seidel algorithm (Beccarelli, 2020). A preliminary comparison with SIMULIA Abaqus 2017 (Dassault Systemes) finite

element software was made to assess the quality of the algorithm, in terms of frictional slips and total energy dissipated per cycle W_l, Eq. (27), see Beccarelli (2020) for details.

5.1. Contact between symmetric elastic bodies

Let us consider the symmetric contact between two elastic blocks of sides $2a$, with $a = 10$mm, Young's modulus $E = 200$GPa and Poisson's coefficient $\nu = 0.3$ (Fig. 8a). External loads consist in a static force $F_3 = -P_o$, which is the resultant of a uniformly distributed pressure applied on the top surface, and cyclic forces F_1, F_2 comprising the resultants of shear tractions Q_1, Q_2 and equilibrating bending moments M_1, M_2. Loads are applied to body 1, whereas body 2 is constrained along its bottom surface to prevent rigid body motion. Finite elements are uniformly spaced along the contact surface with step $0.1a$, for a total of 441 contact nodes. Additionally, we have considered the same geometry and loading but introduced a material mismatch by changing the elastic properties ($E_1 = 200$GPa, $\nu_1 = 0.01, E_2 = 8.73$TPa, $\nu_2 = 0.30$) of the bodies. In the corresponding two-dimensional plane strain problem the material mismatch can be quantified by Dundurs' bimaterial constants (Barber, 2018), which for the selected case are equal to $\alpha_D = 0.96$ and $\beta_D = 0.48$. Notice that the material parameters have been intentionally chosen in order to maximise the effect of the mismatch with respect to contact coupling (Flicek et al., 2017).

In Fig. 8b, the stick and shakedown limits from the linear optimisation algorithm are compared with incremental results for a selected friction coefficient ($f = 0.6$) in the case of elastically similar bodies, which corresponds to an uncoupled contact where $\lambda_2 = \lambda_1$. However, we might notice some

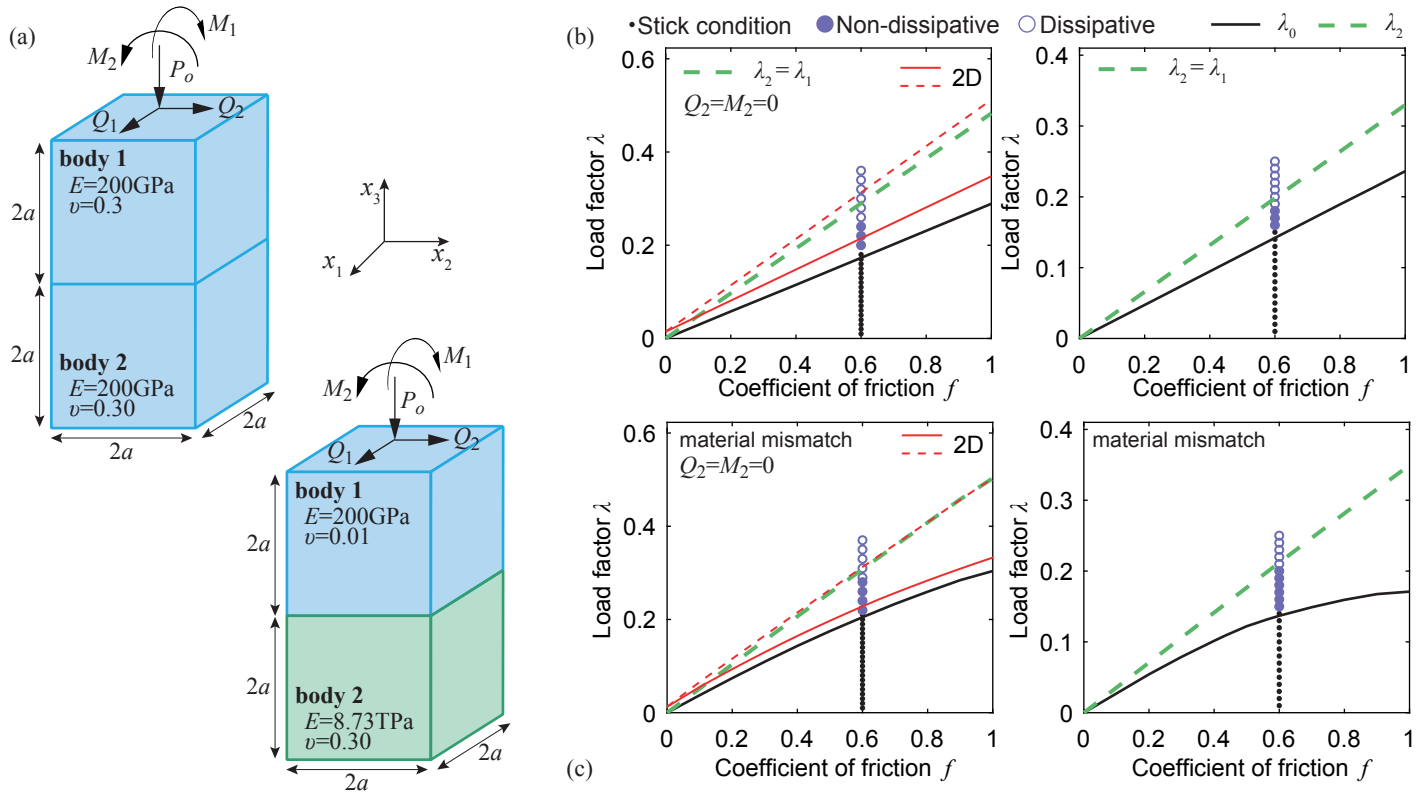

Figure 8. (a) Three-dimensional contact between symmetric bodies, with same elastic properties and material mismatch. Stick and shakedown load multipliers λ_0 and λ_2 from linear optimisation and comparison with results from incremental analyses using the Gauss-Seidel algorithm for $f = 0.6$ in (b) symmetric elastic bodies and (c) bodies with material mismatch. Simulations with load case I ($Q_2 = M_2 = 0$) are compared with the corresponding two-dimensional problem. 2-col figure

discrepancy with the Gauss-Seidel results, presumably due to the piecewise linearisation of Coulomb's cone in the optimisation. As a matter of fact, the normal to the polygon approximating Coulomb's circle in the tangential plane might not be coincident with the direction of the reaction vector $\boldsymbol{r}_t$ (Fig. 2). Furthermore, circumscribed linearisation tends to overestimate the limit condition, while results obtained with inscribed polygonal approximation (not shown here) provided smaller limit loads. In Fig. 8c we report the results for the case with material mismatch, in which the main feature seems

to be a nonlinear variation of the stick limit with respect to the coefficient of friction f. Under load case I, Eq. (26) with $F_2 = 0$, we can also compare the corresponding two-dimensional problem, which appears to show a very similar response both with and without material mismatch. In other terms, the symmetry of the problem is such that coupling between tangential directions is negligible, so that only three-dimensional loading – i.e load case II, Eq. (26), where $F_1 = F_2 \neq 0$ – fully activates the three-dimensional response of the contact.

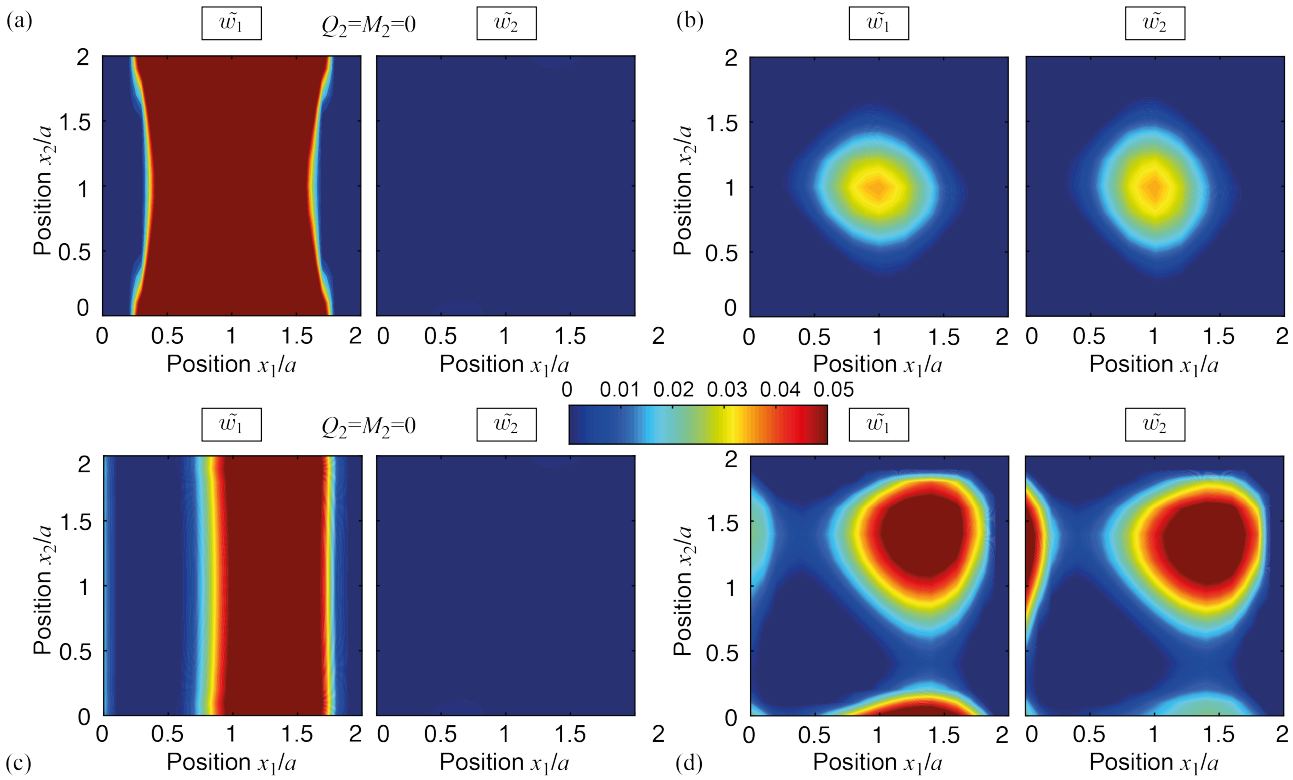

Figure 9. Contours of normalised slips $\tilde{w}_1, \tilde{w}_2$ for $f = 0.6$, obtained from the Gauss-Seidel algorithm for $\lambda = \lambda_2$ (extracted at the last time instant). Uncoupled case with symmetric elastic bodies, (a) load case I and (b) load case II. Bodies with material mismatch, (c) load case I and (d) load case II.2-col figure

In Fig. 9 we show the contours of the dimensionless slips $\tilde{w}_1, \tilde{w}_2$ extracted from the last time step of

incremental analyses, for $f = 0.6$ and $\lambda = \lambda_2$. It appears that loading along x_1 generates a symmetric distribution with maximum along the mid-section of the contact surface ($x_1 = a$), while no slip occurs in the other direction (Fig. 9a). Interestingly, material mismatch seems to break the symmetry, with slips of comparable magnitude but shifted with respect to the mid-section (Fig. 9c). With load case *II*, the uncoupled problem shows a double symmetry, with maximum displacements in the middle, where indeed shear stress is expected to be maximum (Fig. 9b). Once again, the coupled case appears not symmetric (Fig. 9d). We can also compare slips in the uncoupled problem with the optimal $\boldsymbol{w}_{\text{op}}$ distribution computed from linear optimisation and illustrated in Fig. 10. It appears that for load case *I* the trends look very similar (Fig. 10a compared to Fig. 9a), although next to the edges slips $\tilde{w}_{\text{op},1}$ are negative; however, load case *II* portrays a rather complex pattern without an apparent physical relevance (Fig. 10b compared to Fig. 9b).

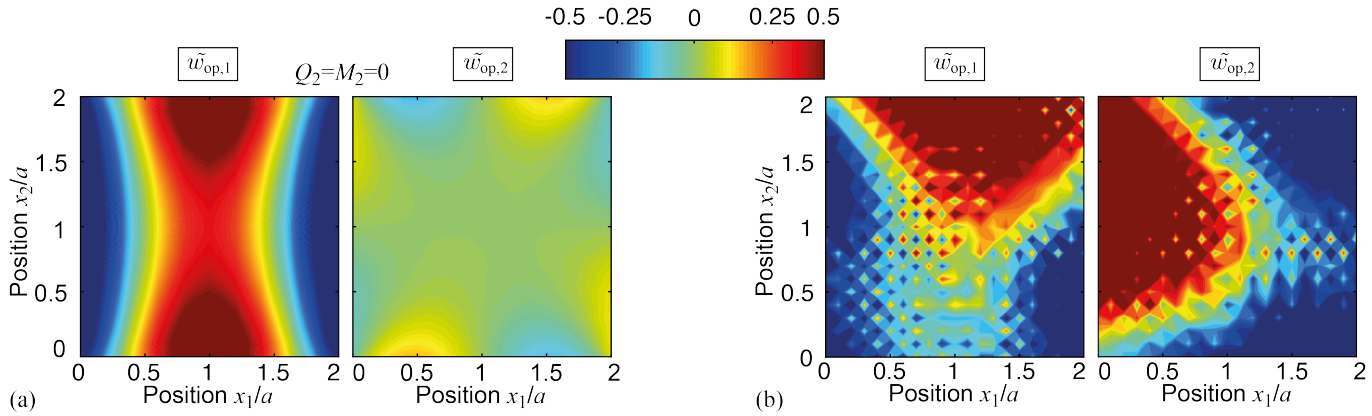

Figure 10. Contours of normalised optimal slips $\tilde{w}_{\text{op},1}, \tilde{w}_{\text{op},2}$ from linear optimisation, for $f = 0.6$, in the uncoupled problem. (a) Load case *I* ($Q_2 = M_2 = 0$) and (b) load case *II*. Please notice the different scale with respect to Fig. 9. 2-col figure

5.2. Contact between punch and half-space

In this section we analyse the three-dimensional contact between a square punch and an elastically similar half-space, approximated by a large rectangular block of sides $20a$ and height $10a$. The material is linear elastic, with Young's modulus $E = 200$GPa and Poisson's coefficient $\nu = 0.3$. $F_3 = -P_o$ is the resultant of a uniformly distributed pressure applied on the top surface of the punch, whereas the tangential components F_1, F_2 consist in uniformly distributed bulk tractions Q_1, Q_2 applied to the half-space (Fig. 11a). The half-space is constrained along its bottom surface to prevent rigid body motion. Finite elements are uniformly spaced along the contact surfaces with step $0.1a$, for a total of 441 contact nodes. Differently from the previous example of symmetric bodies, here the normal-tangential coupling arises because of a domain mismatch, which generally is weaker than that arising from material dissimilarity (Flicek et al., 2017). Because of the mismatch, the state of stress in proximity of the sharp corners presents a singularity, which in the corresponding two-dimensional problem can be computed by means of the asymptotic method in both stick and slip scenarios. However, here the stress might be singular not only along the edges but also at the vertices (Koguchi and Muramoto, 2000). The dominant term in the edge regions provides a lower bound on Coulomb's friction coefficient for the existence of a full adhered solution, with $f = 0.543$ in the two-dimensional problem (Churchman and Hills, 2006; Flicek et al., 2015b). In other terms, when $f \leq 0.543$, a region of edge slip will always be present, implying that a stick limit cannot be properly defined. Indeed, the existence of a lower bound seems to be confirmed in the three-dimensional results derived from the optimisation, as illustrated in Fig.

11b (the two-dimensional problem is added as comparison). Please notice that the critical coefficient of friction differs from the limit predicted by asymptotic analysis, because the mesh refinement is not sufficient to approximate the steep stress gradients in the edge regions.

The contours of the dimensionless slips extracted from the last time step of incremental analyses, for $f = 0.6$ and $\lambda = \lambda_2$, are reported in Fig. 11c. In both load cases, the trend of $\tilde{w}_1$ looks similar, with null values in the mid-section of the contact surface ($x_1 = a$) and an antisymmetric distribution. The same distribution applies to $\tilde{w}_2$ slips in load case II, while these are null everywhere when $Q_2 = 0$. We have also added the optimal slip distributions $\boldsymbol{w}_{\text{op}}$ for comparison (Fig. 11d). It appears that the agreement is rather good, save for the slip distribution parallel to the x_2-direction when $Q_2 = 0$. Finally, Figs. 11e-f show the same comparison between incremental analyses and optimisation results in terms of the slip magnitude, with arrows representing the slip direction on the contact plane.

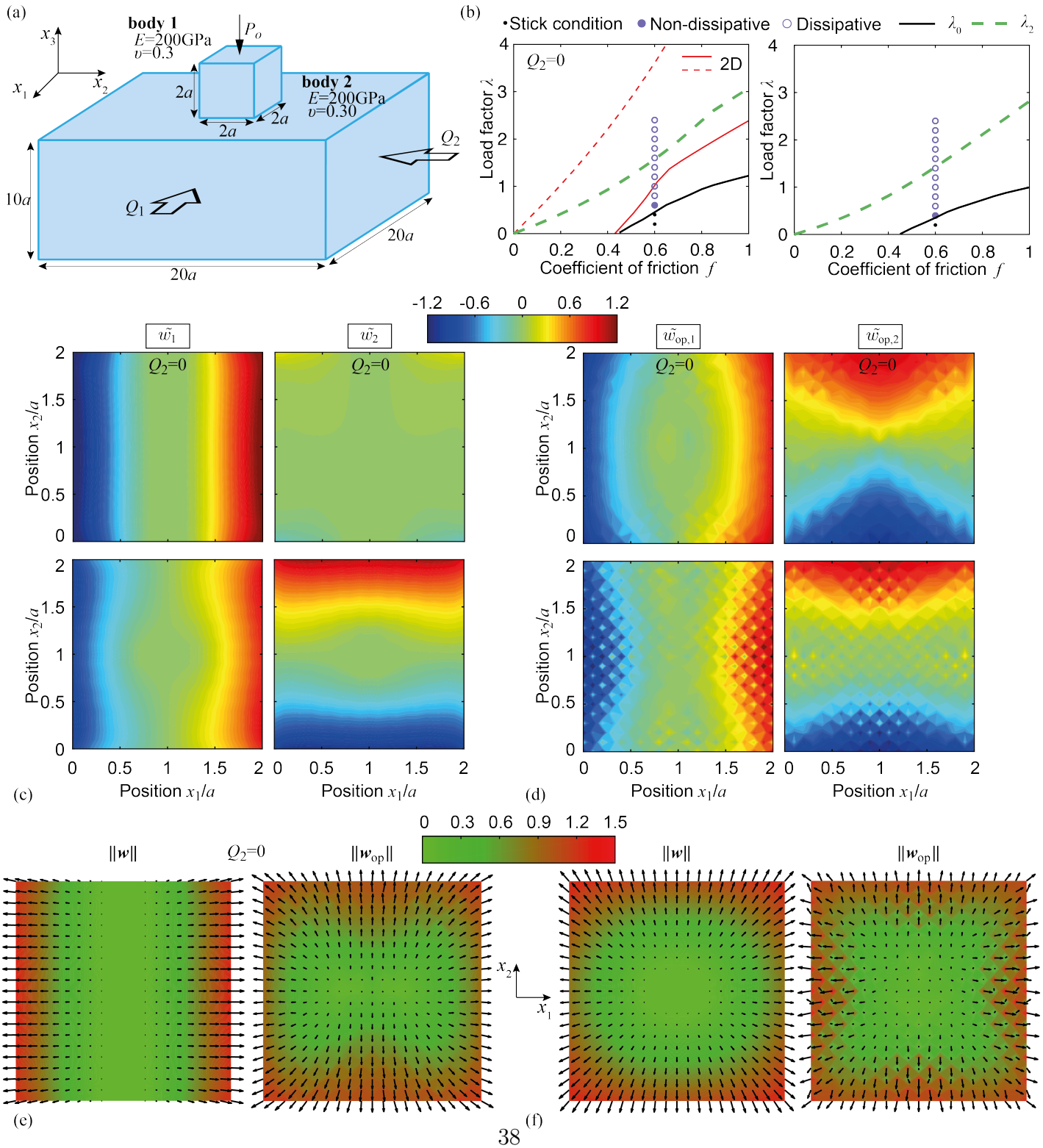

Figure 11. (a) Three-dimensional contact between a square punch and an elastically similar half-space. (b) Stick and shakedown load multipliers λ_0 and λ_2 from linear optimisation and comparison with results from incremental analyses using the Gauss-Seidel algorithm for $f = 0.6$ (related to the three-dimensional problem). Simulations with load case I ($Q_2 = 0$) are compared with the corresponding two-dimensional problem. (c) Contours of normalised slips $\tilde{w}_1, \tilde{w}_2$ for $f = 0.6$, obtained from the Gauss-Seidel algorithm for $\lambda = \lambda_2$ (extracted at the last time instant). (d) Contours of normalised optimal slips $\tilde{w}_{\mathrm{op},1}, \tilde{w}_{\mathrm{op},2}$ from linear optimisation, for $f = 0.6$. (e-f) Contours of normalised slip magnitude $\|\boldsymbol{w}\|$ and $\|\boldsymbol{w}_{\mathrm{op}}\|$ and quiver plots of slip direction on the contact plane x_1, x_2, for both load cases. 2-col figure

6. Discussion

Contact between conforming bodies remains a challenging topic with both theoretical and numerical complexities; often, it has been faced under the simplifying assumption of a two-dimensional domain, where the frictional contact problem has amenable features, including a piecewise linear frictional law. We argue that the main feature of three-dimensional contacts is the existence of coupling in the tangential plane, which activates the fully nonlinear frictional response even in the case of two-dimensional loading. To tackle the complex response of three-dimensional contacts, we have resorted to a single-node system, previously studied by Cho and Barber (1999), which in this work has been considered to analyse the quasi-static response to cyclic loading. The onset of slip and the maximum amplitude of cyclic loads below which a non-dissipative steady state might exist can be easily determined using the proposed optimisation algorithm. More interestingly, we can manipulate the stiffness matrix of the system to explore the impact of contact coupling: indeed, in the most general case, non-zero off-diagonal terms imply that, above the stick limit, displacements and contact reactions in different directions are mutually affected. Comparing a case of full coupling with a tangentially uncoupled system ($\kappa_{21} = 0$), we have clearly shown that the evolution of slips differs, by plotting the trajectory of the node during the whole loading history (Fig. 6). Specifically, a fully coupled system can develop slips in any direction, irrespectively of the direction of loading (squares in Fig. 6a-b).

The impact of tangential coupling on three-dimensional multi-node systems is more difficult to assess. Slip contours obtained from incremental analyses, in both the two-body contact and punch on half-space

problems, suggest that tangential coupling is absent. This is highlighted by the null distribution of slip displacements w_2 when loading is applied along direction x_1 only (Figs. 9a-c, Fig. 11c, top). It might be a reasonable consequence of the symmetry of both problems in the tangential plane (note that the tangential coupling in the problems analysed is strictly connected with the adopted orientation of the coordinate system x_1, x_2 in the contact plane). However, this seems to contradict the considerable difference with respect to the corresponding two-dimensional case in terms of slip limit and shakedown upper bound obtained from the optimisation. In other terms, even when the configuration of the problem results in poor coupling on the tangential plane, the response to external loading is fully three-dimensional.

Normal-tangential contact coupling has a fundamental impact on the assessment of the shakedown limit load. Its main effect is the development of a conditional region in the steady state response, in which dissipative and non-dissipative scenarios might coexist below the shakedown upper bound λ_2, depending on initial conditions. It was out of the scope of our work to explore the impact of different initial conditions within the conditional region, whose size appears to increase with the level of friction (Fig. 5). In general cases, the impossibility of employing limit analyses theorems has made iterative approaches, such as that proposed by Flicek et al. (2017), inevitable. In the case of the single-node system, we have illustrated how the size of the conditional region can be approximated through a didactic example (Fig. 7). Taking advantage of the amenable case of two-dimensional loading and no tangential coupling ($\kappa_{21} = 0$), we have performed an analytical computation of the limits enclosing

all the dissipative scenarios explored with incremental analyses (Fig. 5c). Specifically, we could show that the system is able to sustain cyclic loads up to the dissipative limit $\lambda_D = f$, whereas reaching the shakedown upper bound λ_2 requires different initial conditions with a non-zero slip displacement along the other tangential direction. The same behaviour is observed in multi-node systems as well, with load case I ($Q_2 = 0$), where a notable difference exists between the results of incremental analysis and linear optimisation. Specifically, the dissipative limit λ_D computed from the incremental analysis in the half-space problem (for $f = 0.6$, lower hollow circle in Fig. 11b) is considerably smaller than the shakedown upper bound λ_2 from the optimisation (green dashed line in Fig. 11b). Indeed, this is reflected in the different distribution of slips in the x_2-direction (Fig. 11c compared to Fig. 11d), suggesting that reaching the shakedown upper bound requires a non-zero slip displacement along this direction.

The origin of coupling is debated. In discrete formulations, a measure of coupling can be related to some norms of the the reduced stiffness matrix (Flicek et al., 2017). In our work, we have explored both material and domain mismatch and found an appreciable impact on the limit loads. Theoretical arguments for the impact of material dissimilarity in complete contacts stem from the analysis of Dundurs' bimaterial constants (Barber, 2018). However, the existence of such parameters for the three-dimensional case is debatable (Koguchi and Muramoto, 2000).

7. Conclusion

We have carried out a comprehensive study on the behaviour of three-dimensional systems with conforming frictional contacts subjected to cyclic loading. The numerical tools proposed include an optimisation algorithm to compute the shakedown load multiplier, based on the upper bound theorem for non-associated frictional laws and linearisation of Coulomb's cone. Furthermore, incremental analyses following a prescribed loading history were performed with a Gauss-Seidel algorithm, in a new formulation suitable for the fully nonlinear three-dimensional frictional problem. These approaches are extremely efficient with respect to alternative numerical methods (such as, for instance, finite element analyses) in large-scale discrete problems, taking advantage of a static condensation procedure which reduces the degrees of freedom of any problem to the sole contact nodes. While both the numerical approaches were previously applied to two-dimensional complete contacts, their extension to the full three-dimensional case required a non-trivial effort. The main outcome of our work is the comprehensive picture offered on the response of three-dimensional systems, which we have tried to highlight by including comparisons with the two-dimensional case. Specifically, our results help to shed light on the role of contact coupling, which in three dimensions is enriched with a term deriving from the interaction between reactions and displacements on the contact plane. Under loading histories of constant normal load and pulsating tangential actions, illustrative examples are discussed in terms of the shakedown response. These include: single node systems with different normal and tangential coupling scenarios; symmetric bodies with possible material mismatch; punch on a half-space with domain mismatch. In

conclusion, the numerical algorithms, tested in various geometries, may be efficient tools to support the analyses of contact geometries in engineering applications.

References

Ahn, Y.J., 2015. Shakedown upper limit determination of coupled multi-node discrete frictional systems to cyclic loading. Journal of Mechanical Science and Technology 29, 447–451. doi:10.1007/s12206-015-0104-3.

Ahn, Y.J., Barber, J.R., 2008. Response of frictional receding contact problems to cyclic loading. International Journal of Mechanical Sciences 50, 1519–1525. doi:10.1016/j.ijmecsci.2008.08.003.

Ahn, Y.J., Bertocchi, E., Barber, J.R., 2008. Shakedown of coupled two-dimensional discrete frictional systems. Journal of the Mechanics and Physics of Solids 56, 3433–3440. doi:10.1016/j.jmps.2008.09.003.

Andresen, H., Hills, D., Barber, J., Vázquez, J., 2019. Frictional half-plane contact problems subject to alternating normal and shear loads and tension in the steady state. International Journal of Solids and Structures 168, 166–171. doi:10.1016/j.ijsolstr.2019.03.025.

Antoni, N., 2014. A study of contact non-linearities in pin-loaded lugs: Separation, clearance and frictional slipping effects. International Journal of Non-Linear Mechanics 58, 258–282. doi:10.1016/j.ijnonlinmec.2013.09.007.

Antoni, N., 2017. A further analysis on the analogy between friction and plasticity in Solid Mechanics. International Journal of Engineering Science 121, 34–51. doi:10.1016/j.ijengsci.2017.08.012.

Barber, J.R., 2018. Contact Mechanics. Springer International Publishing, Cham.

Barber, J.R., Klarbring, A., Ciavarella, M., 2008. Shakedown in frictional contact problems for the continuum. Comptes Rendus Mécanique 336, 34–41. doi:10.1016/j.crme.2007.10.013.

Beccarelli, G., 2020. Behaviour of 2D and 3D elastic frictional systems under cyclic loading. Master's thesis (in italian). University of Parma.

Björkman, G., Klarbring, A., 1987. Shakedown and residual stresses in frictional systems, in: Gladwell, G.M.L., Ghonem, H., Kalousek, J. (Ed.), Contact Mechanics and Wear of Rail/Wheel Systems II: Proceedings of the 2nd International Symposium, pp. 27–39.

Carpinteri, A., Scavia, C., 1993. Energy dissipation due to frictional shake-down on a closed crack subjected to shear. Meccanica 28, 347–352. doi:10.1007/BF00987173.

Cho, H., Barber, J.R., 1998. Dynamic behavior and stability of simple frictional systems. Mathematical and Computer Modelling 28, 37–53. doi:10.1016/S0895-7177(98)00107-1.

Cho, H., Barber, J.R., 1999. Stability of the three-dimensional Coulomb friction law. Proceedings of the Royal Society of London. Series A: Mathematical, Physical and Engineering Sciences 455, 839–861. doi:10.1098/rspa.1999.0337.

Churchman, C.M., Hills, D.A., 2006. General results for complete contacts subject to oscillatory shear. Journal of the Mechanics and Physics of Solids 54, 1186–1205. doi:10.1016/j.jmps.2005.12.005.

Churchman, C.M., Korsunsky, A.M., Hills, D.A., 2006. The Application of Plasticity Principles to Friction. The Journal of Strain Analysis for Engineering Design 41, 323–328. doi:10.1243/03093247JSA96.

Drucker, D., 1954. Coulomb friction, plasticity and limit loads. Journal of Applied Mechanics 21, 71–74.

Figueiredo, F.C., Borges, L.A., 2020. Limit analysis and frictional contact: formulation and numerical solution. Meccanica 55, 1347–1363. doi:10.1007/s11012-020-01167-5.

Fleury, R., Hills, D., Ramesh, R., Barber, J., 2017. Incomplete contacts in partial slip subject to varying normal and shear loading, and their representation by asymptotes. Journal of the Mechanics and Physics of Solids 99, 178–191. doi:10.1016/j.jmps.2016.11.016.

Flicek, R.C., Brake, M.R.W., Hills, D.A., 2017. Predicting a contact's sensitivity to initial conditions using metrics of frictional coupling. Tribology International 108, 95–110. doi:10.1016/j.triboint.2016.09.038.

Flicek, R.C., Hills, D.A., Barber, J.R., Dini, D., 2015a. Determination of the shakedown limit for large, discrete frictional systems. European Journal of Mechanics A/Solids 49, 242–250. doi:10.1016/j.euromechsol.2014.08.001.

Flicek, R.C., Hills, D.A., Dini, D., 2015b. Sharp edged contacts subject to fretting: A description of corner behaviour. International Journal of Fatigue 71, 26–34. doi:10.1016/j.ijfatigue.2014.02.015.

Klarbring, A., 1986. A mathematical programming approach to three-dimensional contact problems with friction. Computer Methods in Applied Mechanics and Engineering 58, 175–200. doi:10.1016/0045-7825(86)90095-2.

Klarbring, A., 1990. Examples of non-uniqueness and non-existence of solutions to quasistatic contact problems with friction. Ingenieur-Archiv 60, 529–541. doi:10.1007/BF00541909.

Klarbring, A., Barber, J.R., Spagnoli, A., Terzano, M., 2017. Shakedown of discrete systems involving plasticity and friction. European Journal of Mechanics A/Solids 64, 160–164. doi:10.1016/j.euromechsol.2017.02.006.

Klarbring, A., Ciavarella, M., Barber, J.R., 2007. Shakedown in elastic contact problems with Coulomb friction. International Journal of Solids and Structures 44, 8355–8365.

Koguchi, H., Muramoto, T., 2000. The order of stress singularity near the vertex in three-dimensional joints. International Journal of Solids and Structures 37, 4737–4762. doi:10.1016/S0020-7683(99)00159-6.

König, J.A., Maier, G., 1981. Shakedown analysis of elastoplastic structures: A review of recent developments. Nuclear Engineering and Design 66, 81–95. doi:10.1016/0029-5493(81)90183-7.

Maier, G., 1969. Shakedown theory in perfect elastoplasticity with associated and nonassociated flow-laws: A finite element, linear programming approach. Meccanica 4, 250–260. doi:10.1007/BF02133439.

Majzoobi, G.H., Abbasi, F., 2017. On the Effect of Contact Geometry on Fretting Fatigue Life Under Cyclic Contact Loading. Tribology Letters 65, 125. doi:10.1007/s11249-017-0906-9.

Michalowski, R.L., Mroz, Z., 1978. Associated and non-associated sliding rules in contact friction problems. Archives of Mechanics 30, 259–276.

Mugadu, A., Hills, D.A., 2003. The evolution of the process zone when a complete contact is subject to cyclically varying loads. International Journal of Solids and Structures 40, 4417–4435. doi:10.1016/S0020-7683(03)00184-7.

Nowell, D., Dini, D., Hills, D., 2006. Recent developments in the understanding of fretting fatigue. Engineering Fracture Mechanics 73, 207–222. doi:10.1016/j.engfracmech.2005.01.013.

Ponter, A.R.S., 2016. Shakedown limit theorems for frictional contact on a linear elastic body. European Journal of Mechanics A/Solids 60, 17–27. doi:10.1016/j.euromechsol.2016.05.003.

de Saxcé, G., Bousshine, L., 1998. Limit analysis theorems for implicit standard materials: Application to the unilateral contact with dry friction and the non-associated flow rules in soils and rocks. International Journal of Mechanical Sciences 40, 387–398. doi:10.1016/S0020-7403(97)00058-1.

Spagnoli, A., Terzano, M., Barber, J.R., Klarbring, A., 2017. Non-linear programming in shakedown

analysis with plasticity and friction. Journal of the Mechanics and Physics of Solids 104, 71–83. doi:10.1016/j.jmps.2017.04.006.

Thaitirarot, A., Flicek, R.C., Hills, D.A., Barber, J.R., 2014. The use of static reduction in the finite element solution of two-dimensional frictional contact problems. Proceedings of the Institution of Mechanical Engineers, Part C: Journal of Mechanical Engineering Science 228, 1474–1487. doi:10.1177/0954406213509086.